

1 **Beyond and beneath displacement time series: towards InSAR-based early warnings and**
2 **deformation analysis of the Achoma landslide, Peru**

3

4 Benedetta Dini^{1,2}, Pascal Lacroix², Marie-Pierre Doin²

5 ¹School of Geography, Earth and Environmental Sciences, University of Birmingham, Birmingham, UK

6 ²ISterre, Université Grenoble-Alpes, Grenoble, France

7

8 Corresponding author:

9 Benedetta Dini, School of Geography, Earth and Environmental Sciences, University of Birmingham,
10 Birmingham, UK

11 Formerly at: ISterre, Université Grenoble-Alpes, Grenoble, France

12 orcid number: 0000-0002-1578-7294

13 Email address: b.dini@bham.ac.uk

14

15 **Abstract**

16 Detecting precursors to slope destabilisation with sufficient lead time and accuracy remains
17 a challenging and unresolved issue in landslide hazard assessment and prediction. This is key,
18 as catastrophic landslides often go unnoticed until immediately before or after failure,
19 limiting opportunities for intervention. While in situ methods offer high accuracy at point
20 locations, they are costly and require prior knowledge of instability. Satellite-based synthetic
21 aperture radar differential interferometry (InSAR) has shown promise in identifying unknown
22 landslides over large areas and has been proposed as a potentially useful tool for failure
23 prediction. Typically valued for retrieving displacement time series, InSAR time series
24 reliability depends heavily on successful interferogram unwrapping, which often leads to
25 severe underestimations over landslides. Here, we analyse the deformation process of the
26 Achoma landslide in Peru and demonstrate that the InSAR signal contains precursors based
27 on alternative markers, even without displacement time series. Interferometric coherence
28 shows the formation of gravitational structures up to five years before failure, as well as a
29 critical shift in landslide behaviour three months prior to failure. Additionally, a marker based
30 on the wrapped phase reveals and quantifies alternating periods of quiescence and motion,
31 the latter becoming more frequent in the two years before failure. Our findings highlight the
32 potential to use alternative InSAR signal markers to observe the deformation process and

33 progressive failure leading up to the event, and to detect landslide precursors across
34 extensive areas, providing valuable lead time for intervention and disaster prevention.

35

36 **Keywords:**

37 InSAR - Landslide precursors – Incipient slope destabilisation - Early warning indicators
38 Progressive failure – Landslide dynamics – Interferometric coherence - Interferometric
39 wrapped phase

40

41 **1. Introduction**

42 Landslides pose a global threat, causing more than 4000 fatalities annually (Petley 2012)
43 including more than 4,000 resulting from non-seismic triggers (Froude and Petley 2018).
44 Beyond the human toll, landslides lead to substantial social and economic consequences in
45 both developing and developed countries. Despite advances in hazard assessment, predicting
46 when and where potentially unstable hillslopes will fail catastrophically remains a major
47 challenge. This highlights the critical importance of early identification of destabilizing slopes
48 and the detection of accelerating phases, which are key to improving prediction and
49 preparedness (e.g., Carlà et al. 2017a; Roy et al. 2022; Valletta et al. 2022; Strząbała et al.
50 2024).

51 While there are documented instances of successful predictions and early warnings using in-
52 situ methods (e.g., Badoux et al. 2009; Loew et al. 2017; Fan et al. 2019), two main challenges
53 persist: cost and feasibility of monitoring all known unstable slopes, and the limited pre-
54 existing knowledge of instability, which often leads to landslides remaining unnoticed until
55 severe acceleration or catastrophic failure occurs (Palmer 2017; Guzzetti 2021), causing
56 significant delays in the installation of monitoring systems (e.g., Fiolleau et al. 2020).

57 The advent and use of satellite-based technologies, particularly satellite-based synthetic
58 aperture radar differential interferometry (InSAR), have significantly improved landslide
59 identification capabilities (e.g. Strząbała et al. 2024). Observations can be made more cost-
60 effectively due to the increasing availability, frequency, and reliability of acquisitions, whilst
61 the large coverage (Costantini et al. 2021; Lacroix et al. 2021; Wasowski and Bovenga 2022)
62 may allow for the identification of previously unknown unstable slopes at large scales (Dini et
63 al. 2019, 2020). This enhances the possibility of implementing timely and targeted monitoring

64 before disasters occur. Identifying destabilising slopes from satellite data is crucial also for
65 landslides in remote locations, which are challenging to spot and monitor in-situ, yet can
66 generate far-reaching hazard cascades (Cook et al. 2021). With increasing temporal sampling
67 of new generation satellites (e.g. Sentinel-1) and the potential for sub-centimetre
68 displacement accuracy in favourable conditions (Ferretti et al. 2011; Liu et al. 2013; Wasowski
69 and Bovenga 2014), the use of InSAR has become widespread for generating landslide
70 displacements time series based on small baseline subset (Berardino et al. 2002) (SBAS) or
71 permanent scatterers (Ferretti et al. 2001, 2005) (PS) algorithms, and variations of these. In a
72 few cases, retrospective retrieval of time series revealed acceleration patterns leading to
73 failure, highlighting potential for accurate prediction of failure timing (Intrieri et al. 2018;
74 Carlà et al. 2019).

75 However, despite InSAR's remarkable potential for geohazard observation, the universal
76 reliability of InSAR displacement time series is not guaranteed, due to significant challenges
77 related to the nature of the phenomena and data processing limitations. We highlight here
78 only the limitations relevant to this work. For a more exhaustive account we refer to Lacroix
79 et al. (2021) and references therein.

80 Small to medium-size landslides (a few tens to a few hundred m along-scarp length) in many
81 cases only cover a relatively small number of SAR pixels on the ground (e.g., for the pixel size
82 of Sentinel-1, 2.3 m by 14.1 m), making signal detection challenging. Moreover, not all
83 landslides are expected to exhibit measurable precursory deformation prior to failure.
84 Rapid, shallow landslides in loose materials may fail abruptly with no significant
85 precursors. Larger landslides (several hundred m along-scarp length) may exhibit
86 displacements only on isolated sectors at different times. Additionally, landslides often
87 present strong spatial gradients and sharp displacement edges (e.g. Cheaib et al., 2022) that
88 make phase unwrapping problematic due to phase aliasing (Manconi 2021; Strz̧abała et al.
89 2024). Finally, landslides often display non-linear behaviour in time, with phases of
90 accelerations interspersed with periods of quiescence. This is unfavourable for InSAR time
91 series based on SBAS or PS approaches (e.g. Handwerker et al., 2025), particularly when
92 temporal sampling is affected by missing acquisitions or unusable images (e.g., snow cover,
93 seasonal landcover changes). When a slope transitions from no displacement to fast
94 reactivation, with displacements exceeding a threshold (commonly $\frac{1}{4}$ of the wavelength)
95 between two acquisitions and/or between adjacent pixels when gradients are strong, phase

96 aliasing and decorrelation occur. The lack of phase continuity makes it difficult to accurately
97 reconstruct the continuous phase signal from the wrapped phase measurements. As
98 conventional processing methods for generating displacement time series rely on phase
99 unwrapping, they are particularly susceptible to phase aliasing (Manconi 2021). Moreover, as
100 interferometric coherence decreases, unwrapping over critical areas might not be performed
101 when processing large areas due to the cutoff imposed using coherence thresholds. This leads
102 to the loss of any true deformation signal potentially contained in low- (or lower-) coherence
103 interferograms. In essence, the success on landslide of common InSAR approaches heavily
104 relies on the existence of many conditions favourable to processing. Without individual
105 interferogram inspection, a time consuming task, an InSAR displacement time series might
106 seem accurate and plausible, yet it could significantly underestimate the true displacements
107 and obscure crucial acceleration phases and/or their magnitude (Dini et al. 2020; Jacquemart
108 and Tiampo 2021). Consequently, there is a high potential for misinterpreting the ongoing
109 processes driving instability and assessing the hazard level.

110 In response to the challenges associated with InSAR, some authors focused on the analysis of
111 high temporal frequency optical images (e.g., Sentinel-2, PlanetLab) to derive time series of
112 displacements (Lacroix et al. 2018, 2023), or changes in vegetation cover caused by landslides
113 with NDVI from Sentinel-2 acquisitions (Yang et al. 2019). However, optical data are
114 constrained by cloud coverage and have limited sensitivity to smaller displacements that
115 might occur over longer time frames leading up to failure. Others have successfully retrieved
116 acceleration phases through image correlation of SAR images (Li et al. 2020), but this method
117 is also limited to the observation of relatively large displacements (greater than 1/10 of the
118 pixel size), thus more suitable to cover the final weeks to months of an accelerating phase.
119 Consequently, alternative and/or complementary InSAR-based techniques must be
120 developed to improve our ability to observe landslide precursors beyond what is possible
121 using only methods reliant on phase unwrapping. Jacquemart et al. (2021) focused on InSAR
122 coherence, showing a temporal decrease of coherence roughly 5 months prior to the
123 Mudcreek landslide failure. To our knowledge this is the only study on this topic, highlighting
124 the need for more case-studies and in-depth understanding of landslide behaviours
125 associated with this type of signal. Since rapid, shallow landslides may fail without
126 measurable precursors, coherence-based approaches are likely most effective for

127 larger, slower, or more complex landslides where deformation evolves progressively over
128 time.

129 Our work introduces a novel methodology for extracting landslide precursors that bypasses
130 traditional time series generation. Instead, we integrate information on incipient and ongoing
131 instability using interferometric coherence and wrapped phase. This approach is particularly
132 valuable when full displacement time series are unavailable or unreliable. By addressing the
133 limitations of conventional methods, we offer an alternative perspective on landslide
134 precursor identification from space. This paper explores two critical questions: Can
135 interferometric coherence serve as an effective precursor for identifying critical landslide
136 phases and incipient instability in both time and space? And can indicators based on the
137 wrapped phase provide insights into criticality of landslide behaviour, in the absence of a
138 reliable displacement time series?

139 To illustrate our methodology, we present a case study on the Achoma landslide in the Colca
140 Valley, Peru. This landslide exemplifies an instability that remained unnoticed on the ground
141 until shortly before catastrophic failure, while retrospective analysis using optical satellite
142 images detected signals three months before the event (Lacroix et al. 2023). Although our
143 analysis is retrospective, the signals identified represent genuine precursory indicators detectable in
144 the InSAR data before failure. Remarkably, our results show that signs of destabilisation were
145 detectable five years prior to failure. The subsequent sections of this paper detail the methods
146 we employed, including topographic error correction, coherence loss analysis, and the
147 extraction of wrapped phase temporal behaviour. Finally, we present our results and discuss
148 their significance, highlighting the potential integration of our approach with traditional
149 methods.

150

151 **2. Study area**

152 The deeply incised Colca Valley is located in southern Peru. On its terraces, it hosts several
153 settlements, largely supported by extensive agriculture. The valley is located between
154 volcanic massifs to the north and south (Zerathe et al. 2016), and is characterised by
155 sequences of ignimbrites and pyroclastic deposits. The valley's geomorphology has been
156 shaped by debris avalanches from valley flank collapses followed by landslide dam breakouts

157 (Thouret et al. 2007), with one such event forming a paleolake and depositing thick lacustrine
158 deposits(Lacroix et al. 2015; Zerathe et al. 2016).

159 Seismicity in the region has distinct sources (Zerathe et al. 2016; Lacroix et al. 2023 and
160 references therein), from relatively low magnitude ($M_w < 3$) seismic events originating in the
161 volcanic area approximately 15-20 km to the southwest, to larger magnitude earthquakes
162 associated with regional tectonic faults ($M_w < 7$) or $M_w 8$ events with origin in the subduction
163 zone roughly 100 km to the west.

164 The area experiences a seasonal climate pattern, with most of the rainfall falling between
165 December and April(Lacroix et al. 2015), followed by a dry season. Annual rainfall amounts
166 range between 350 and 600 mm, with daily cumulative precipitation rarely exceeding 25 mm.
167 Numerous large landslides dot the Colca valley (Pham et al. 2018), often showing
168 retrogressive failure in the lacustrine deposits (Zerathe et al. 2016) and responding to
169 different trigger mechanisms (Lacroix et al. 2015, 2023; Bontemps et al. 2020). Persistent
170 uncertainties surround the factors controlling their evolution into slow or rapid landslides
171 (Zerathe et al. 2016), making the evaluation of their hazard potential difficult. Other landslides
172 in the valley that have been long creeping have been instrumented for years (Lacroix et al.
173 2014, 2015; Palmer 2017; Bontemps et al. 2020) , providing valuable insights into landslide
174 dynamics and responses to seismic and climatic triggers.

175 The Achoma landslide, failed catastrophically on 18th June 2020, unnoticed for a long time
176 until cracks were reported by locals in May 2020 (Dini et al. 2022; Lacroix et al. 2023), only
177 one month prior to failure. It is a large and deep-seated landslide that spans approximately
178 800 m in width along its scarp and extends 500 m downslope to the Colca River, covering an
179 area of about 0.4 km² (Figure 1). The headscarp rises approximately 100 m high (Lacroix et al.
180 2023), with estimated rupture surface depth averaging 50 m. The landslide volume is thus
181 estimated at around $20 \times 10^6 \text{ m}^3$.

182 The failure occurred during the dry season, following cumulative rainfall of 600 mm during
183 the preceding wet season. Earlier findings indicated the landslide gradually accelerated three
184 months before its failure, initiating during the rainy season (Lacroix et al. 2023), suggesting
185 rainfall may have played a crucial role in the transition from slow to rapid movement. The site

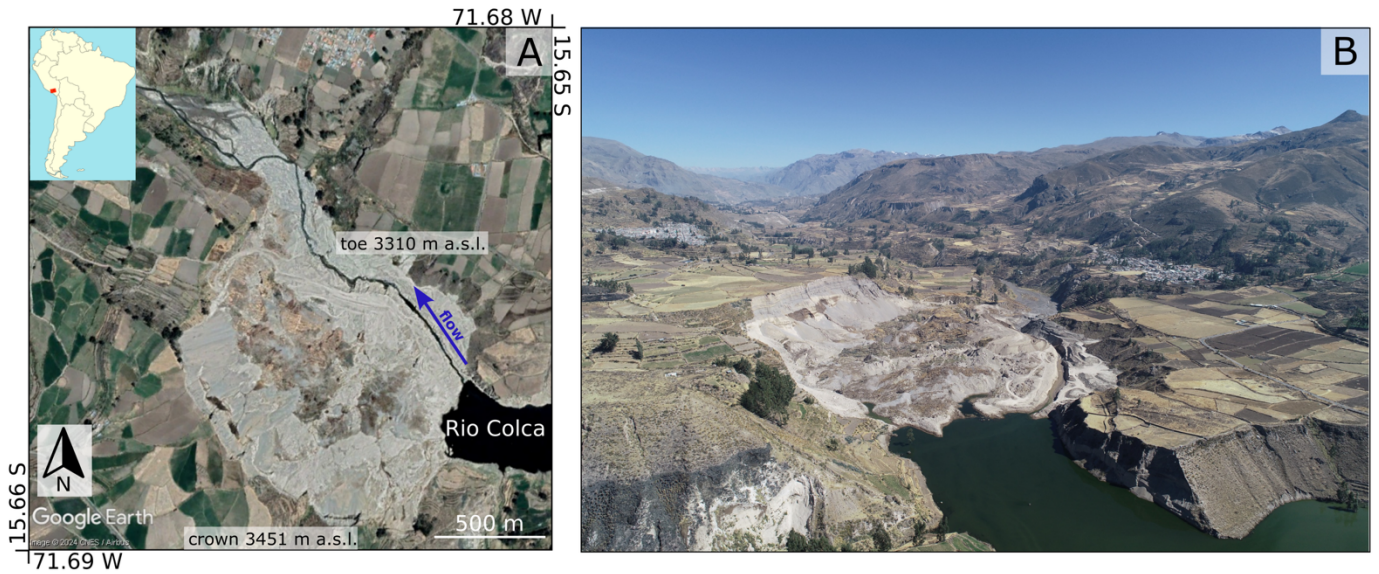


Figure 1. A) Study area, Achoma landslide post failure (©GoogleEarth Image, CNES/Airbus 1/11/2020). Red rectangle in top left inset shows footprint of Sentinel 1 images (relative orbit number 47). B) Drone image of the landslide, looking northwest. Credits: Ingemmet.

186 has experienced seismic activity during the observation period, with the largest earthquake
 187 recorded on 15th August 2016, measuring Mw 5.5 (Bontemps et al. 2020).

188

189 3. Methods and data

190 3.1. Raw interferograms

191 We generated 514 Sentinel-1 wrapped interferograms from 114 satellite acquisitions of
 192 ascending track with relative orbit number 47, covering the period between 30th April 2015
 193 and 20th June 2020 (the rupture of the Achoma landslide occurred the 18th of June) over the
 194 Colca Valley, Peru. The interferograms were generated with the NSBAS processing chain (Doin
 195 et al. 2011), at medium spatial resolution. Sentinel-1 data, originally acquired with a ground
 196 resolution of 2.3 m in range and 14 m in azimuth, were multilooked (8 and 2 looks in range
 197 and azimuth, respectively) to a final pixel size of 18.4 m × 28.2 m. Temporal baselines range
 198 from 12 days (the minimum available for the area) to 1 year. The topographic contribution of
 199 the signal was removed with the SRTM 30m digital elevation model. The interferograms were
 200 not filtered, in order to avoid possible artefacts and loss of deformation signal (Strozzi et al.
 201 2020).

202 A first inspection of the interferograms was carried out, this revealed a non-linear behaviour
 203 of the landslide, characterised by phases of quiescence and activity. The nature of the
 204 landcover, largely composed of agricultural land and the intermittent, occasionally strong

205 displacement gradients cause low coherence and low signal to noise (S/N) ratios in
 206 interferograms with temporal baselines of 48 days and longer. The highest signal-to-noise
 207 (S/N) ratios are observed for temporal baselines of 12 and 24 days. Thus, for the successive
 208 analyses described in the following sections, we selected a series of 113 successive
 209 interferograms with the shortest available baselines. Additionally, we included
 210 interferograms with baselines of 30, 48, and 72 days to cover periods where shorter baselines
 211 are unavailable due to missing images (Supplementary Figures S1-S8). Whilst this approach
 212 does not offer the redundancy of image connections required for time series inversion, it
 213 allows to cover the observation window with the highest S/N ratio interferograms, whilst
 214 limiting the number of gaps over the period.

215

216 The boundaries of the Achoma landslide were mapped in geographical coordinates based on
 217 geomorphological characteristics observed on Google Earth optical images (Dini et al. 2022).
 218 The polygon outline was then projected in the geometry of the radar images. The
 219 interferograms were cropped around the landslide polygon, with the crop size (71 by 81
 220 pixels) chosen to provide a margin around the landslide in each direction comparable in size
 221 to the landslide itself. This allows for a meaningful comparison between the area inside the
 222 landslide and the surroundings as well as for the presence of areas assumed stable (not
 223 affected by displacements) and characterised by good temporal interferometric coherence
 224 (equal to or higher than 0.4). A 5 x 5 pixels window was used to calculate coherence, γ , as:

225

$$\gamma = \frac{|\langle S_1 \cdot S_2^* \rangle|}{\sqrt{\langle S_1 \cdot S_1^* \rangle \langle S_2 \cdot S_2^* \rangle}} \quad (1)$$

226

227 where $\langle \cdot \rangle$ is the complex conjugation averaged over the chosen window and S_1 and S_2 are the
 228 complex values of primary and secondary images composing an interferogram (Kumar and
 229 Venkataraman 2011; Dini et al. 2022).

230

231 In the following sections, we illustrate: 1) the removal of the component of the phase signal
 232 proportional to perpendicular baselines from the raw interferograms, to identify and mitigate
 233 any residual component associated with topographic errors; 2) the analysis of coherence loss

234 patterns; 3) the analysis of the raw phase signal and its changes over time; and 4) the analysis
235 of the influence of seismicity, rainfall, and river erosion on the landslide's recent history.

236

237

238

239 3.2. Topographic error correction of raw interferograms

240 An area assumed stable (i.e., not affected by ground displacements) was chosen outside the
241 landslide boundaries. Various window sizes were tested for this area, and a 5 x 5 pixel window
242 was ultimately chosen—large enough to provide a more meaningful average of phase values
243 than a single pixel, yet small enough to avoid including areas with markedly different ground
244 reflectivity. The choice of the window was based on the average of a proxy of the temporal
245 coherence, as defined by Thollard et al. (2021), ensuring phase stability, this was followed by
246 a visual analysis of the geomorphological features in the proximity of the landslide. The phase
247 of each wrapped interferogram (prior to landslide failure) was referenced to the mean phase
248 of the selected stable reference window, $e^{i\varphi_{k,ref}}$, computed for each interferogram, k , by
249 multiplying the interferometric phase of all pixels by the complex conjugate of the average
250 phase within the reference window (Dini et al. 2022). After this referencing step, the influence
251 of the perpendicular baseline on the phase values of individual pixels within each
252 interferogram was analysed. Higher perpendicular baselines cause higher sensitivity to
253 topography (Colesanti and Wasowski 2006; Meyer and Sandwell 2012), therefore, if
254 topographic residuals exist after the topographic component removal with the SRTM digital
255 elevation model, a correlation between baselines and interferometric phase would be
256 revealed. Such topographic residual might be associated with low DEM accuracy or changes
257 of ground surface occurred after DEM acquisition and prior to SAR images acquisition. To do
258 this, we computed the average phase over 5 x 5 moving windows, l , over the entire crop,
259 noted $e^{i\varphi_{k,l}}$. To account for the circular nature of phase values (modulo 2π), a parameter
260 search was carried out to determine the best linear fit within the complex domain. For each
261 moving window, predicted values were calculated as:

$$e^{i\widehat{\delta\varphi}_{k,l}} = e^{iX_k\beta_l} \quad (2)$$

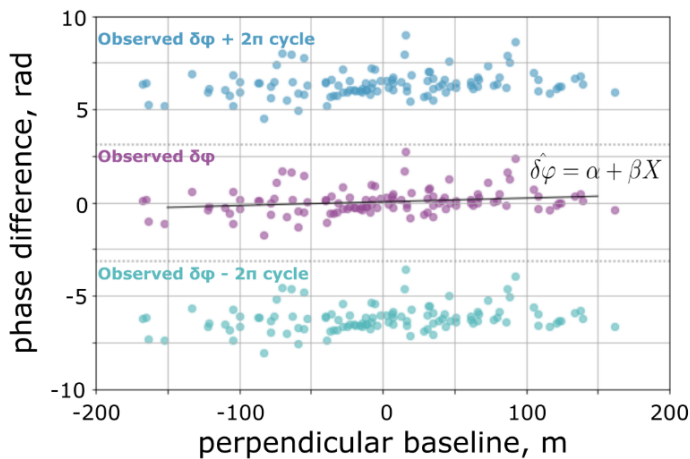
262

263 where $e^{i\widehat{\delta\varphi}_{k,l}}$ is the predicted phase in each window l of interferogram k , X_k is the
264 perpendicular baseline of each interferogram and β_l is the proportionality coefficient

265 between $e^{i\delta\varphi_{k,l}}$ and the perpendicular baseline for the window l (Dini et al. 2022). During the
 266 parameter search, multiple bounds for β were tested before selecting -0.5 and 0.5 rad/m, with
 267 a step size of 0.001. The value of β is determined by maximising the coherence ρ_k between
 268 the predicted and observed values given by:

$$\rho_k = \left| \frac{\sum_k e^{i\varphi_{k,l}} * e^{i\widehat{\delta\varphi_{k,l}}}^*}{N} \right| \quad (3)$$

269 where N is the number of interferograms (Dini et al. 2022). Maps of β , ρ and corrected
 270 interferograms were generated. An example of the relationship between phase and
 271 perpendicular baseline for all interferograms is shown in figure 2.
 272



273 **Figure 2.** Example of correlation between phase and perpendicular baseline for one moving window. Each purple point
 represents the complex average phase in the sample window for a given interferogram with respect to the complex average
 phase in the reference area. As the phase is known in modulo 2π , its $+2\pi$ and -2π values are also shown in blue and teal
 respectively. (Modified from Dini et al. 2022, Gretsli Colloque Proceedings).

274 3.3. Coherence loss analysis

275 Interferometric coherence and its changes within the landslide and in the surrounding area
 276 were analysed both in space and time, in a qualitative and quantitative way respectively. We
 277 retained all the selected 113 successive interferograms for this analysis, irrespective of their
 278 average coherence. This is because if coherence is to be used as a precursory indicator, its
 279 potential should be tested over a range of interferograms, including those in which the phase
 280 might be unreliable. Spatial coherence loss is identified within individual interferograms. We
 281 focused on patterns of coherence loss over confined areas, as a proxy of localised strain:
 282 localised and spatially organised changes of the complex interferometric values are likely
 283

284 associated with localised displacements, particularly if these correspond to gravitational
285 morphological features (e.g. scarps or extensional structures associated with gravitational
286 slope movements).

287 In order to detect changes in mean coherence through time and between the landslide and
288 the surrounding gravitationally stable areas, we first calculated for each interferogram the
289 average coherence over the whole crop, along the scarp and within the mapped landslide
290 boundaries. The scarp and crown areas are key locations for precursory detection as motion
291 related to retrogression might be focused here. Boundaries for the scarp were mapped on
292 Google Earth optical images on the basis of geomorphological features and then converted in
293 radar coordinates, as for the landslide boundaries. We analysed the average coherence time
294 series in relation to daily rainfall, downloaded from the online platform of the national service
295 of Meteorology and Hydrology of Peru (Servicio Nacional de Meteorología e Hidrología del
296 Perú) (see section 3.6.2 for further details). We then computed the time series of the ratio
297 between average landslide coherence and average coherence of the surrounding area
298 (Jacquemart and Tiampo 2021). The ratio is chosen because it highlights changes occurring in
299 the landslide with respect to the surroundings, whilst accounting for periods of coherence
300 loss associated to vegetation changes or ground moisture changes due to rainfall events that
301 would affect the coherence everywhere in a similar way. The changes highlighted by such
302 ratio are therefore most likely associated with ongoing deformation inside the landslide area.
303 In our method, coherence is interpreted relative to a local surrounding area rather than across
304 a large region or the entire SAR frame. As mentioned in section 3.1, we selected the size of
305 the surrounding area so that it is comparable to the landslide footprint, serving as a baseline
306 for normal variability, but not too large to avoid including very different noise sources. Thus,
307 this approach does not require the landslide to stand out across a much larger area; rather,
308 the key signal emerges from local deviations detectable over a few km scale. A temporal
309 mean coherence was computed for each pixel and compared to background terrain
310 using z-scores (see supplementary material and Supplementary Figure S9).

311 312 3.4. Wrapped phase analysis

313 As explained in section 1, the presence of interferograms with a high displacement gradient
314 and/or low S/N ratio hinders the ability to perform reliable phase unwrapping without errors
315 during phases of landslide acceleration. We thus adopted the following procedure to analyse

316 the wrapped phase signal in time, whilst avoiding phase unwrapping. Following an approach
 317 similar to that presented in López-Quiroz et al. (2009), we selected 5 interferograms
 318 characterised by high S/N ratio and by relatively low displacement gradients. In particular, we
 319 ensured to select only interferograms in which the observed displacements gradients would
 320 not exceed 2π over the landslide area. The visual inspection of all wrapped interferograms
 321 revealed that the area affected by displacements has a similar spatial pattern until failure and
 322 that the displacement gradient, as observed in interferograms with higher S/N ratio, has the
 323 same sign throughout (which is expected in gravitational motion). For the five chosen
 324 interferograms we added 2π to all pixels with phase value < -1 rad, thus obtaining a pattern
 325 with values comprised between -1 and 5.28 rad. We then averaged these interferograms,
 326 obtaining what we will refer as a model deformation pattern (Figure 3A). We cut the area
 327 closely around the deformation pattern over 33 by 33 pixels, in order to reduce the
 328 contribution of noise in the surrounding area. We then used this model pattern to investigate
 329 its correlation with all 113 interferograms in the series, so that:

330

$$e^{i\widehat{\delta\varphi}_{k,p}} = e^{iM_p\alpha_k} \quad (4)$$

331

332 where $e^{i\widehat{\delta\varphi}_{k,p}}$ is the predicted phase value at pixel p of interferogram k , M_p is the phase value
 333 of the model deformation pattern at pixel p and α_k is the proportionality coefficient between

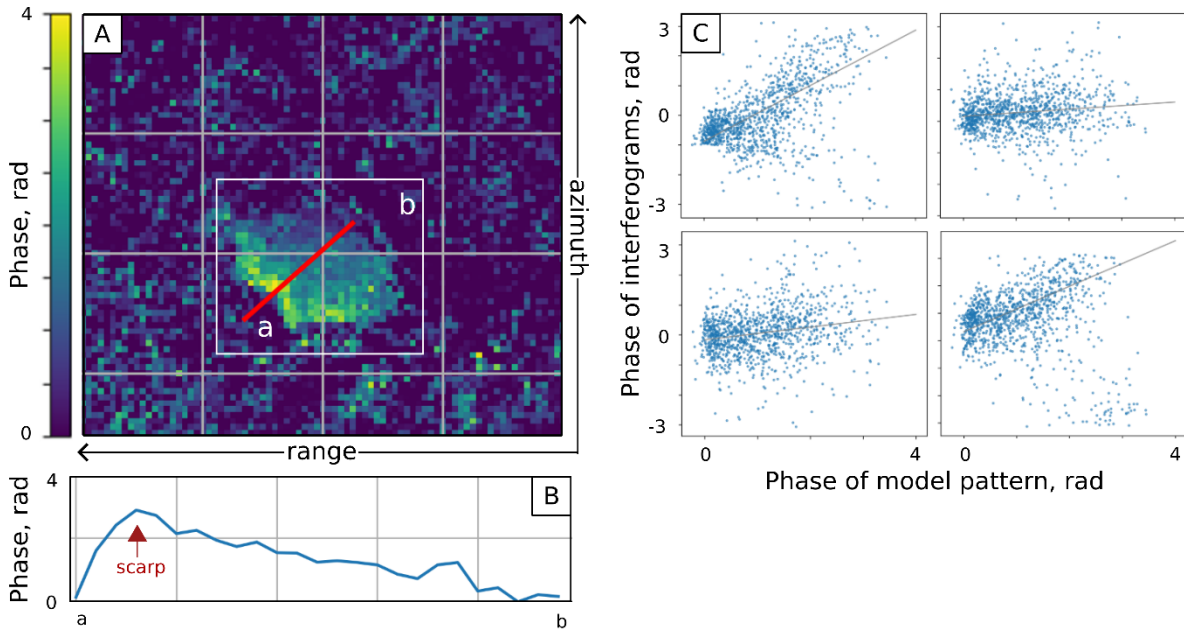


Figure 3. A) Model pattern of deformation in radar coordinates (flipped left-right); B) model pattern phase gradient for the profile a-b; C) examples of four interferograms showing the pixel-by-pixel correlation with the model pattern (from top left, clockwise: 18/08/2018-30/08/2018, 30/08/2018-11/09/2018, 23/09/2018-05/10/2018, 05-10/2018-29/10/2018).

334 the phase of the model pattern and interferogram k (Figure 3B). For the parameter search, -
 335 7 and 7 were chosen as bounds for α_k , to account for potentially large displacements that
 336 might have affected the landslide in the days/weeks before failure, with a 0.001 step. The
 337 value of the proportionality coefficient α_k is then used to represent a dimensionless measure
 338 of displacement rates, DI , which is a quantity of activity for each interferogram in the series.
 339 For example, interferograms characterised by α_k around zero are those with no detectable
 340 displacements, whilst α_k around 1 would indicate for interferogram k a similar displacement
 341 gradient to the model pattern. The value of α_k is obtained by maximising the coherence
 342 between the predicted and observed values, the latter a measure of the goodness of fit:

343

$$\gamma_k = \left| \frac{\sum_k e^{i\varphi_{k,p}} * e^{i\widehat{\varphi}_{k,p}}}{N_p} \right| \quad (5)$$

344

345 where N_p is the number of pixels in interferogram k . Successively, the same procedure was
 346 applied only to pixels falling within the landslide, masking outside pixels. This was done to
 347 generate a ratio between the best coherence calculated over landslide pixels only and the
 348 coherence over all pixels, including surrounding area pixels. A low ratio indicates poor fit of

349 the model within the landslide area in particular, which in turn indicates high likelihood of
350 high displacements gradients leading to spatial aliasing and decorrelation. A threshold of such
351 ratio was set at one standard deviation below the mean value. Unreliable interferograms
352 (grey dots in figure 6) are those with ratio falling below this threshold.

353

354 3.5. InSAR-derived downslope displacements

355 The dimensionless measure of displacement rates, DI , obtained with the analysis of raw phase
356 in successive interferograms described in section 2.4 is not an absolute measure of
357 displacements. It represents the degree of activity within the landslide in the time interval
358 covered by each interferogram, as it reflects the correlation between the model pattern and
359 each interferogram. Figure 3C shows a profile across the model that runs along the maximum
360 slope gradient roughly, through the middle of the landslide. The highest values are observed
361 at the scarp, with a maximum value, r_{max} , of 3.45 radians, decreasing to around zero at the
362 toe of the landslide. Therefore, to estimate line of sight (LOS) displacements in mm, we
363 rescaled the dimensionless displacement rates, DI , as:

364

$$DI_{mm} = DI * r_{max} * \frac{\lambda}{2\pi} \quad (6)$$

365

366 where λ is the half the wavelength of the satellite, which for Sentinel-1 is 28 mm.

367 An assumption generally accepted for landslides is that the displacement vector is oriented
368 along a line of maximum slope gradient (Notti et al. 2012). This reflects the overall motion of
369 the landslide, even if, unless the landslide is a pure translational slide, some parts of
370 compound landslides have higher vertical component of the displacements than others.
371 Following the approach presented in Notti et al. (2012), we computed a coefficient that
372 describes the percentage of downslope displacement that is detectable along the line of sight
373 and applied a correction to the displacements. This coefficient is 0.88, for an incidence angle
374 over the area of 40.7 degrees, a heading angle of 347 degrees, and average slope and aspect
375 of 17 degrees and 74 degrees respectively.

376 We then applied a correction to the displacements obtained with the optical image
377 correlation, DO , described in section 2.4, once again assuming that the displacements occur
378 along the maximum slope gradient and taking an average slope angle of 20 degrees, so that:

379

$$DO_{mm} = \frac{DO}{\sin(\vartheta)} \quad (7)$$

380

381 where ϑ is 70 degrees, the complementary to the average slope angle.

382 Finally, we identified the onset of activity periods in the InSAR time series, we fitted for each
383 period a linear model. We then computed the slope of the curve for each phase and compared
384 the values at different ones.

385

386 3.6. External forcing

387 In order to detect external events that may have played a role in the onset of activity at
388 specific times, we took into consideration seismicity, rainfall and maximum river width as a
389 proxy for erosion. The pore pressure increase associated with rainfall (Carey et al. 2019;
390 Agliardi et al. 2020) and seismic shaking (Lacroix et al. 2022a) is an important factor that
391 perturbs the internal stress state of the rupture surface of large landslides, inducing slip onset
392 (Agliardi et al. 2020). River erosion also plays a role in modulating landslide activity in the
393 region (Lacroix et al. 2015) and increased fluvial erosion might increase landslide activity by
394 removing material at the toe (McColl 2022), undercutting the slope (Ballantyne 1986;
395 Fourniadis et al. 2007; Yang et al. 2021) and potentially exposing the sliding surface.

396

397 3.6.1. Earthquakes

398 We computed a comprehensive list of earthquakes with magnitude 3 and above, occurred
399 within a radius of 150 km of the Achoma landslide, between 2015 and July 2020 from the
400 online platform of the Geophysical Institute of Peru's (Instituto Geofísico del Peru). The list
401 comprises of 361 events. For each event, we calculated the expected peak ground
402 acceleration (PGA, m/s^2) as indicator of seismic ground motion at the Achoma landslide site
403 by applying the ground motion prediction method of Akkar and Bommer (2010). This method
404 was shown by previous studies to perform well for a landslide site located approximately 10
405 km west of the Achoma landslide (Lacroix et al. 2015; Bontemps et al. 2020). PGAs of $0.1 m/s^2$
406 and above are obtained for earthquakes occurred at less than 50 km from the landslide, with
407 magnitudes comprised between 3.8 and 5.6, except for one event, occurred at 84 km, but
408 with magnitude 6.2.

409

410 3.6.2. Rainfall

411 Hourly rainfall data starting from 2015 recorded at the station of Chivay, approximately 9 km
412 northeast of the landslide site, at a similar elevation, were downloaded from the online
413 platform of the National Service of Meteorology and Hydrology of Peru. This was then
414 converted into daily rainfall totals. Cumulative rainfall for each dry-rainy season sequence
415 (August to August of following year) has been plotted for every year, to compare activity rates
416 with rainfall. 2015 and 2016 were characterised by drier conditions than following years. To
417 identify more intense daily rainfall events, characterised by higher 24 hours cumulative
418 rainfall, we computed the histogram of daily rainfall, which presents a skewed right
419 distribution. We selected a threshold of 25 mm/day as the intense rainfall event, as
420 frequencies of higher daily totals do not exceed 1 in the whole observation period.

421

422 3.6.3. River erosion

423 As a proxy for river erosion at the landslide's toe, we analysed the changes in river width over
424 time. To accomplish this, we utilised 219 Planet Lab PlanetScope images with 3m ground
425 resolution. We selected three sections along the river: one in the middle of the landslide and
426 one at each boundary. For each image, we measured the river's width at each of the three
427 locations. The river's width broadly follows a seasonal pattern corresponding to the seasonal
428 rainfall over the area, implying that the river's erosive power follows a similar temporal
429 pattern to the rainfall. However, our objective was to identify unseasonably large river events
430 that might be triggered by localised events upstream in the catchment, which are not directly
431 recorded at the nearby meteorological station. To identify such unseasonable events, we
432 computed a rolling mean of the river width and looked for peaks exceeding one standard
433 deviation from the mean. In addition to this, we mapped the riverbanks at maximum width
434 for each year, to determine any position changes through time that might be indicative of
435 persistent, significant erosion.

436

437 4. Results

438 4.1. Spatial coherence features as long-term precursors

439 Interferometric coherence maps generated for all selected successive interferograms (see
440 section 2) exhibit distinct, consistent features over the observation period (figure 4). Notably,
441 low coherence lineaments appear intermittently up to 5 years before the landslide failure.

442 These features manifest as narrow, rope-like structures located primarily along the scarp and
 443 southeastern flank of the landslide, consistent with post-failure observations. Interestingly,
 444 these features persist even in interferograms characterised by generally low coherence,
 445 where phase unwrapping would typically be unreliable. They are identifiable in 25
 446 interferograms spanning from the earliest available (covering the period 30th April 2015 to
 447 11th July 2015) up until 16th March 2020, approximately three months prior to the failure.
 448 Pixels intersecting the scarp exhibit significantly lower coherence than the surrounding
 449 area (Welch's t-test, $p < 0.001$; see supplementary materials and Supplementary Figure
 450 S9). Starting from 9th April 2020 the entire area affected by the landslide shows a more
 451 widespread loss of coherence, indicative of a regime shift.
 452

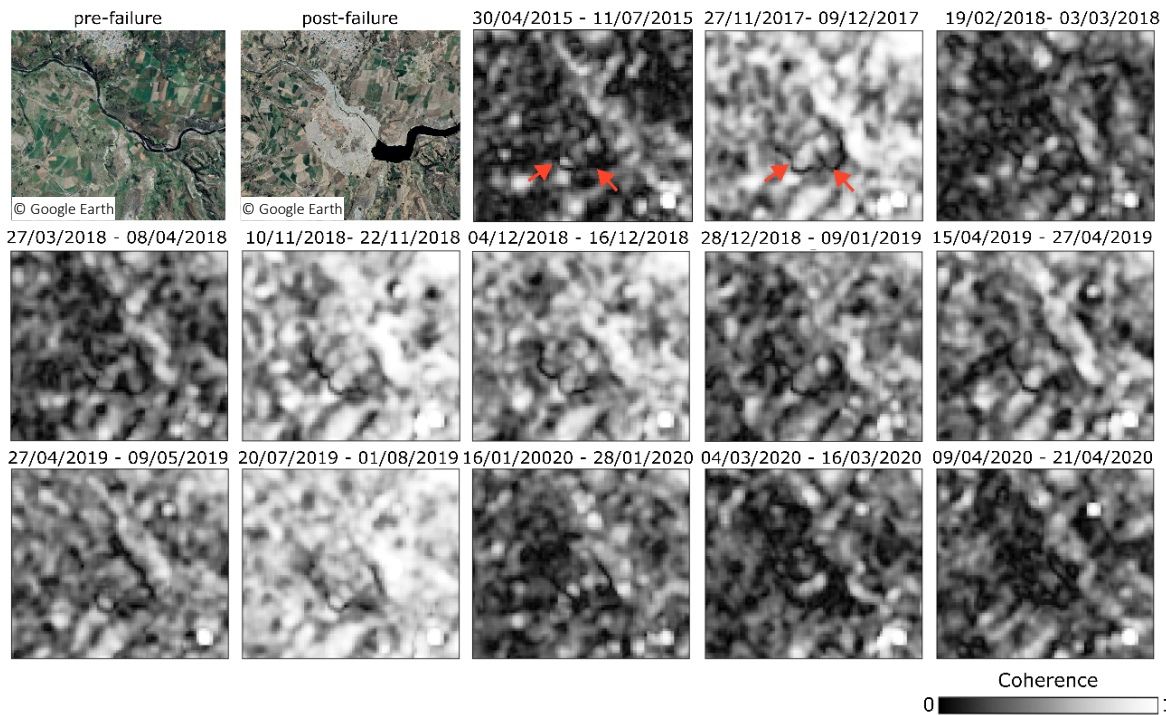


Figure 4. Pre- and post-failure ©Google Earth pre-failure (29/04/2019) and post-failure images (1/11/2020), with a series of interferometric coherence examples showing the development of headscarp and southern boundary, with the change in regime from March 2020.

453

454 4.2. Time series of coherence ratio

455 Figure 5A illustrates the average coherence in the landslide area and in the surrounding area.
 456 Albeit with some small differences, the coherence drops everywhere following similar
 457 temporal patterns during the rainy seasons. The coherence ratio between the landslide and
 458 the surrounding area (figure 5B) remains around 1, with a mean of 0.98, from 30th April 2015

459 to 28th March 2020, encompassing multiple wet seasons. Subsequently, starting from this
 460 date until the failure on 18th June 2020, the ratio progressively declines below 0.8, reaching
 461 its lowest value of 0.19 at the time of failure. The significant drop in the coherence ratio three
 462 months prior to failure indicates that the landslide area was losing coherence faster than its
 463 immediate and directly comparable surroundings.

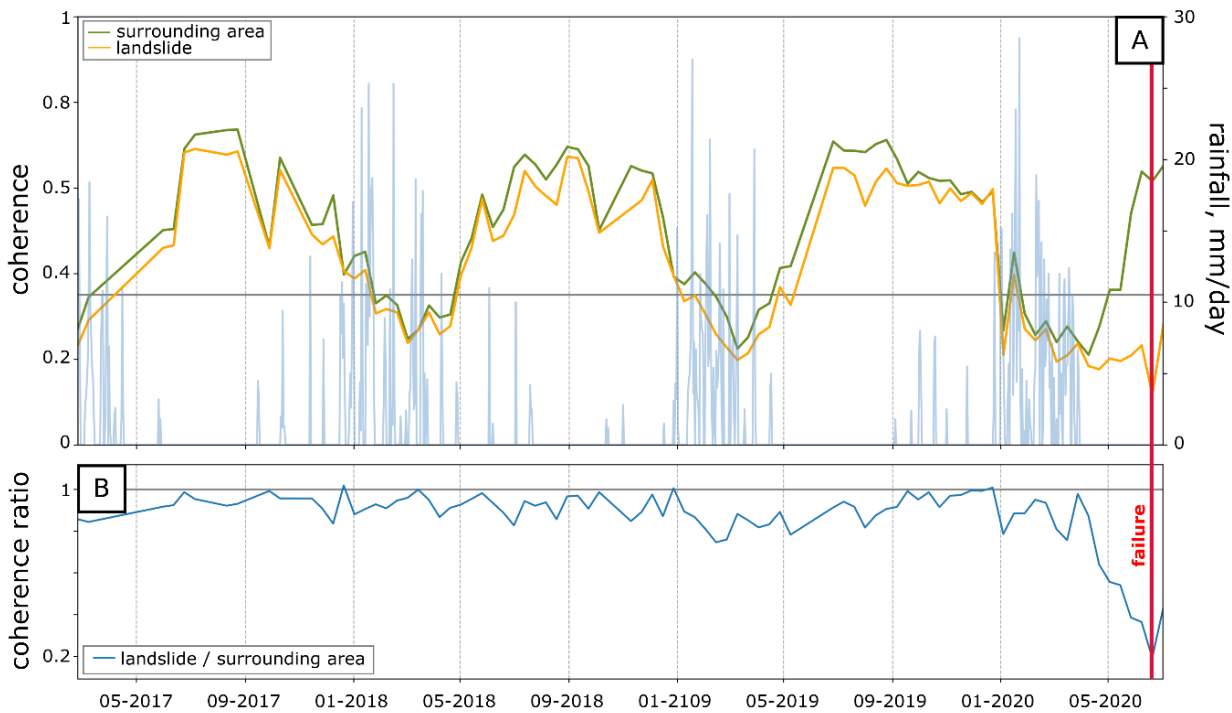


Figure 5. A) Interferometric coherence for different parts of the landslide, superposed on daily rainfall. B) Coherence ratio. Failure is indicated by the vertical red line.

464

465

466 4.3. Acceleration phases as seen by InSAR

467 The dimensionless activity index time series, derived using the method outlined in section 2.5,
 468 is shown in figure 6. The time series reveals periods of relative stability interspersed with
 469 phases of acceleration. Transient creep events are characterised by displacements occurring
 470 within individual or, in one case, over two consecutive interferograms amid periods of
 471 minimal long-term displacements. Four transient creep events between April 2015 and
 472 August 2016 exhibit dimensionless displacement rates exceeding 1, occurring amidst a
 473 backdrop of rates generally around 0 and less than 0.25 (Figure 6; Table 1). The displacements
 474 observed in these interferograms match or exceed the mean deformation pattern shown in

475 figure 3A. In contrast, we observe long acceleration phases, periods during which
 476 displacement rates increase significantly over three successive interferograms or more. These
 477 become apparent from November 2017 onwards.

478 Four distinct acceleration phases are observed:

- 479 • Phase 1: 27th November 2017, to 8th April 2018
- 480 • Phase 2: 19th June 2018, to 9th May 2019
- 481 • Phase 3: 8th July 2019, to 20th July 2019
- 482 • Phase 4: 4th January 2020, to 4th March 2020 (culminating in failure 3 months later)

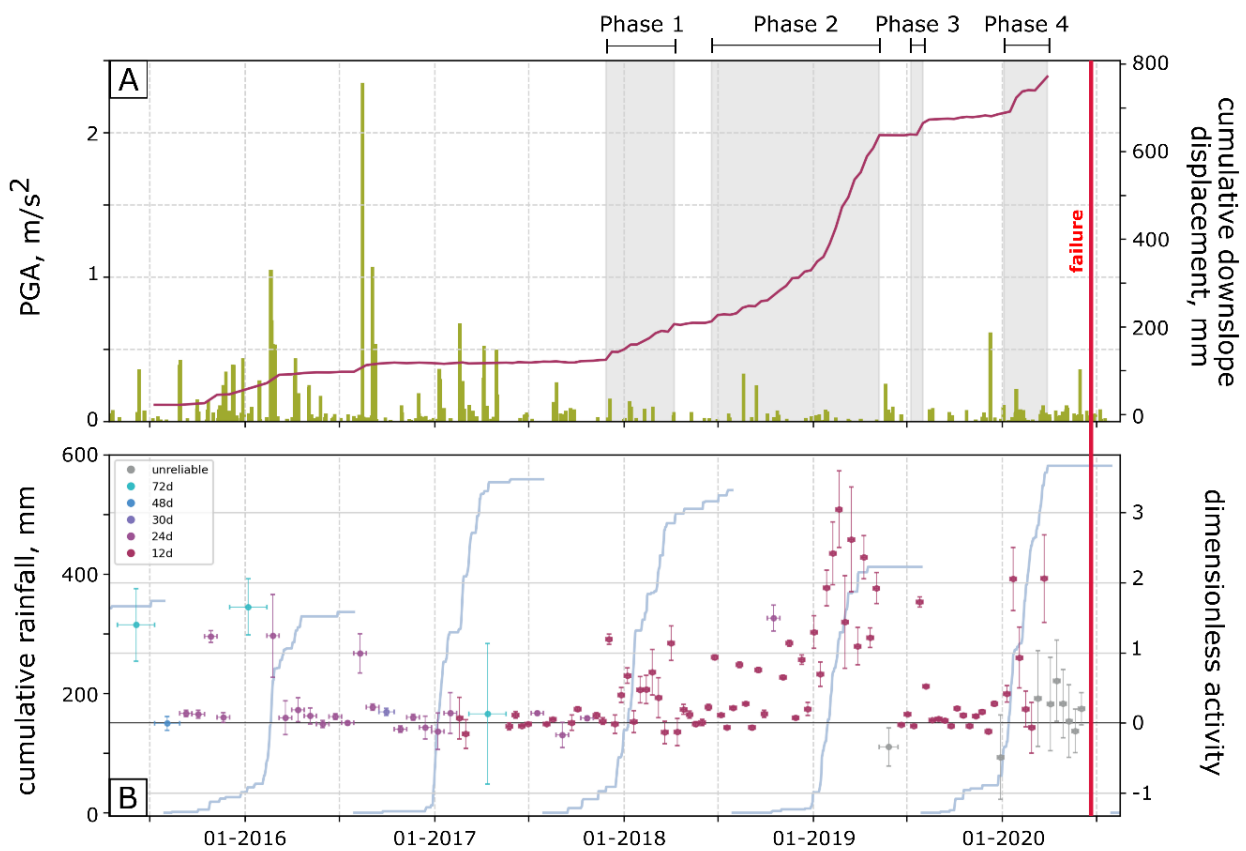


Figure 6. A) purple curve, estimated downslope cumulative displacement in mm after correction; green bars, PGA. B) dimensionless activity index, every dot represents an interferogram, different colours and horizontal bars represent interferogram duration, vertical bars $1/\gamma_k$ normalised by its max value (eq 5); blue curves, cumulative rainfall over the rainy season.

483 The accelerations are detected using the dimensionless index (see section 2.4), but we
 484 present below the estimated rates (see section 2.5), for ease of description.

485 The first acceleration begins with an initial significant displacement (~18 mm in 12 days),
486 followed by a period of linear displacements over 132 days at an almost steady rate of
487 approximately 279 mm/year.

488 The second phase follows a 10-week quiescence period and exhibits escalating trends: 234
489 mm/year between 19th June 2018, and 5th October 2018; 425 mm/year between 5th October
490 2018, and 9th January 2019; and 1080 mm/year between 9th January 2019, and 9th May 2019.

491 A short acceleration in July 2019 transitions quickly into a brief period stability followed by a
492 phase of low, steady-rate creep from 1st August 2019 to 23rd December 2019, characterised
493 by a gentle trend of 38 mm/year. This is succeeded by the last acceleration phase, reaching
494 approximately 567 mm/year from 4th January 2020 to 4th March 2020, the last reliable
495 interferogram captured, then culminating in failure.

496

497 **5. Discussion**

498 5.1. Spatial patterns of low coherence

499 The coherence maps derived from successive interferograms reveal slope instability by
500 delineating gravitational morphological structures dating back five years before failure. In the
501 earliest available interferogram (30th April 2015 – 11th November 2015), a distinct low
502 coherence boundary is evident despite the low average coherence, closely mirroring the later
503 spatial development of the landslide. The low-coherence markers likely indicate areas of
504 strain resulting from landslide displacement, marking the boundary between stable and
505 unstable ground. These markers are interpreted as early signs of destabilisation, suggesting
506 strain concentration along the failure surface is beginning to occur, albeit with very small
507 displacements. We observed similar features in other landslides in the Colca Valley, indicating
508 that these signals are not isolated occurrences and highlighting their importance and
509 reliability for early detection at large scales. Some of these landslides have exhibited long-
510 term creep without progressing to catastrophic failure. In these cases, low-coherence
511 markers appear to indicate retrogressive behaviour with the formation of secondary scarps
512 over the years and delimiting different activity sectors.

513

514 5.2. Factors influencing coherence loss

515 Low interferometric coherence, reflecting high phase variability between adjacent pixels, can
516 be caused by factors like dense vegetation, crops, surface debris, snow, or spatial
517 heterogeneity of ground deformation. In the case of the Achoma landslide, the low coherence
518 markers observed are unlikely to be caused by localised land cover changes. Instead, they
519 likely reflect slight differential displacements associated with the development of surface
520 discontinuities. These features have been observed up to three months before failure, similar
521 to the final acceleration stage detected with optical images by Lacroix et al. (2023).
522 Jacquemart et al. (2021) discuss various factors contributing to interferometric coherence loss
523 in landslides, including soil moisture changes, erosion, vegetation dynamics, and active slope
524 deformation. While distinguishing between these causes is challenging, their combined
525 presence suggests increased landslide activity.

526 The observed transition in coherence patterns, from localised anomalies along gravitational
527 structures to widespread loss across the entire landslide area in March 2020, points to
528 significant shift in landslide dynamics. This likely marks the transition from small
529 displacements (with the landslide behaving as a cohesive body) to higher displacement
530 gradients and internal deformation. Identifying such transitions in coherence could provide
531 valuable lead time for early warnings, offering a proactive approach to landslide monitoring
532 in previously unmonitored areas.

533

534 5.3. Coherence ratio analysis

535 In addition to the spatial patterns of low coherence, we analysed the ratio between the mean
536 coherence over the landslide area and that in the surrounding area, using a methodology
537 similar to that adopted by Jacquemart and Tiampo (2021). This ratio helps account for
538 temporal coherence variability that affects both the landslide and its surroundings similarly.
539 For example, seasonal moisture changes can impact coherence, but the ratio remains close
540 to 1 unless changes occur specifically within the landslide area.

541 A noticeable drop in the coherence ratio occurred approximately three months before the
542 failure event, beginning around 4th March 2020. By setting a retrospective threshold (one
543 standard deviation below the mean coherence ratio), we identified that this threshold was
544 surpassed between 9th and 21st April 2020, indicating predictive value about two months
545 before the Achoma failure. Jacquemart and Tiampo (2021) noted a similar coherence ratio
546 decline approximately five months before the Mudcreek landslide, attributing it partly to

547 vegetation degradation. In contrast, our analysis of the Achoma landslide shows a sharp
548 increase in the coherence ratio post-failure, reaching values as high as 1.98 during the 2021
549 rainy season. This increase suggests that vegetation degradation following the failure may
550 expose rock and soil, enhancing phase stability in the absence of displacements. Thus, the
551 observed drop in coherence leading up to failure is likely associated with high displacement
552 gradients leading to increased internal deformation of the landslide mass and phase aliasing.
553 This observation is consistent with the three-month final acceleration stage identified
554 through independent measurements by Lacroix et al. (2023). Further investigation into other
555 case studies is needed to establish universal indicators and thresholds for landslides at critical
556 stages.

557

558 5.4. Dimensionless activity index

559 The InSAR data processed in this work indicates that the Achoma landslide underwent a long
560 evolution. Our observations show that progressive damage and fault maturation over a
561 period of at least five years, likely longer, ultimately led to landslide failure, in agreement with
562 the findings of Lacroix et al. (2023). To simplify, we separately discuss two broad periods,
563 based on different styles of activity observed.

564

565 *April 2015 to December 2017*

566 The key observation is that between April 2015 and December 2017 the long-term activity
567 index for this period reveals short-lived transient creep events in response to perturbations,
568 interspersed with prolonged period of little to no activity (Figure 6; Table 1). This suggests the
569 presence at this stage of a maturing surface of rupture, allowing for some hydro-mechanical
570 fluid-solid coupling (Agliardi et al. 2020), but not yet a self-sustaining process of progressive
571 failure. Displacements during this period may span up to 72 days due to sampling intervals.
572 Between December 2015 and March 2016, a combination of moderate seismicity and rainfall
573 led to possible prolonged displacements over two consecutive interferograms for up to 96
574 days. However, the temporal resolution of the data does not allow us to determine whether
575 movement was continuous or intermittent within these intervals.

576 While the August 2016 earthquake, with the highest PGA of 2.34 m/s^2 recorded during the
577 study period, did result in some movement, it was lower than the movements observed
578 between April 2015 and March 2016. Moreover, although the rainy season of 2016/2017

579 recorded comparable precipitation totals to subsequent seasons, no prolonged period of
580 acceleration was observed until the end of 2017. This suggests that a combination of
581 seismicity and rainfall may be more critical for driving significant acceleration than either
582 factor alone. Unlike the Maca landslide, which exhibited prolonged post-seismic accelerations
583 following the 20 February and 15 August 2016 earthquakes, lasting 5 months and several
584 weeks, respectively (Bontemps et al. 2020), the Achoma landslide's response was transient
585 and not sustained, as no subsequent interferograms indicated continued movement. Post-
586 seismic motion has been associated to pore-water pressure increases due to sediment
587 contraction (Lacroix et al. 2022a). The absence of post-seismic motion at the Achoma landslide
588 may reflect that the rupture surface was not sufficiently mature, and lacked the necessary
589 pathways for water to migrate from contracted sediments to the rupture zone. Without this
590 migration, the pore pressure at the rupture surface could not build up to a level that would
591 sustain post-seismic motion.

592

Interferogram dates (and duration in days)	Max PGA m/s ²	Number seismic events	Dimensionless displacement (estimate mm)	Estimate displacement rate mm/yr	Cumulative rainfall mm
30/04/2015 – 11/07/2015 (72)	0.36	6	1.4 (~26)	~132	9.1
15/10/2015 – 08/11/2015 (24)	0.15	4	1.2 (~23)	~350	13.1
02/12/2015 – 12/02/2016 (72)	0.44	26	1.7 (~31)	~157	56.4
12/02/2016 – 07/03/2016 (24)	1.05	9	1.2 (~23)	~350	160.1
29/07/2016 – 22/08/2016 (24)	2.34	7	1 (~18)	~274	0

593 **Table 1.** Interferograms showing possible transient creep behaviour associated with nearby earthquakes.

594

595

596 *December 2017 to June 2020*

597 A shift in behaviour can be identified from December 2017: from this point, longer periods of
598 activity begin to occur. The landslide reacts quickly to the onset of the wet season in
599 December 2017, despite lower seismicity than in the previous period, suggesting that the
600 rupture surface has fully developed and become more sensitive to perturbations. This likely
601 reflects the formation of a fine-grained gouge along the basal shear plane (Agliardi et al.
602 2020), reducing permeability and altering pore pressure dynamics. These internal changes led
603 to cycles of acceleration, deceleration, and steady-state stages (Zhou et al. 2018) (Figure 6A),
604 driven by transient perturbations like seismic events or rainfall and modulated by
605 mechanisms like pore pressure dissipation (Lacroix et al., 2020) or strain-strengthening

606 behaviour (Agliardi et al. 2020) ultimately resulting in sustained slip rates even during dry
 607 periods. This pattern is particularly evident during the dry season of 2018, when the Achoma
 608 landslide exhibited sustained displacement rates despite the absence of significant external
 609 triggers. This observation highlights the role of ongoing internal processes, such as continued
 610 damage accumulation along the basal shear plane, in maintaining instability and movement
 611 over time.

612 As Lacroix et al. (2023) note, the final stage of acceleration began in the wet season. While
 613 optical images from Lacroix et al. (2023) pinpoint the beginning of the final acceleration in
 614 March 2020, InSAR-based observations in this study suggest that the landslide began
 615 accelerating as early as January 2020, following a period of steady slip rates during 2019.
 616 Although rainfall was undoubtedly a key factor, similar rainfall totals in 2017 and 2018 did not
 617 lead to failure, suggesting that other factors, such as accumulated damage or changes in the
 618 basal shear zone, were more critical in 2020. Increased seismic activity in the final stages,
 619 marked by a higher frequency of smaller earthquakes, likely contributed to the landslide's
 620 acceleration, demonstrating a combination of driving factors.

621

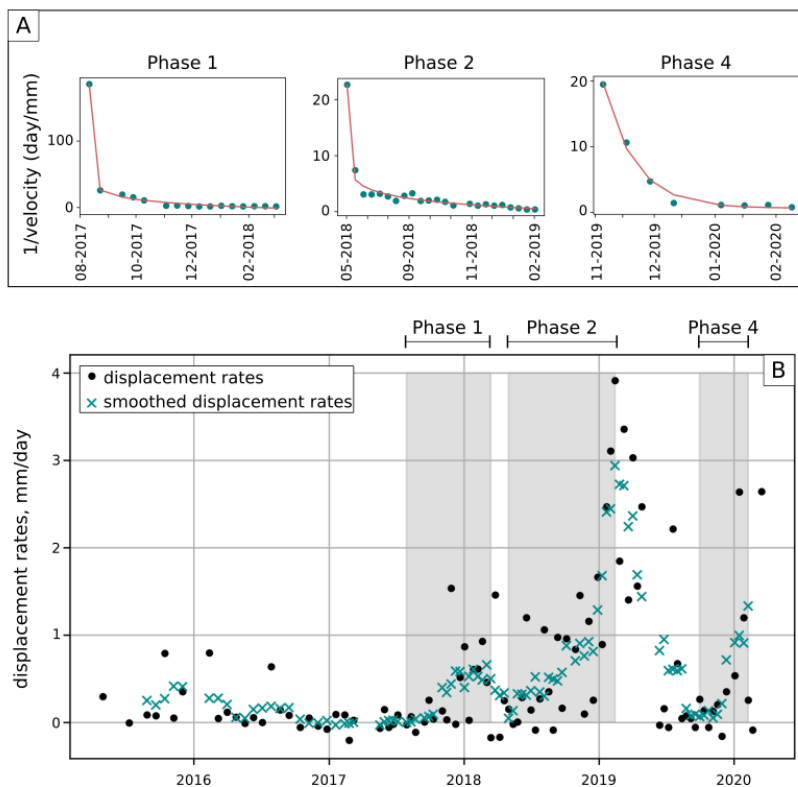


Figure 7. A) $1/\text{velocity}$ plots for phase 1, phase 2, and phase 4. B) Displacement rates for raw (black dots) and smoothed data (blue x, smoothed using a 5-window running mean). Shaded areas show accelerations of phase 1, phase 2 and phase 4.

622 Figure 7 compares acceleration phases 1, 2, and 4 using inverse velocity (day/mm) plots,
623 derived from the estimated displacements. Although the measure is not an absolute
624 displacement, its evolution reflects distinct kinematic behaviours. Phase 1 begins at a high
625 inverse velocity (>100 day/mm), indicating very slow initial movement and a large relative
626 change during acceleration. Phases 2 and 4 start from lower $1/v$ values, suggesting a more
627 active baseline state by the time acceleration began. Phases 1 and 2 show an abrupt initial
628 drop followed by flattening at values above zero, consistent with asymptotic decay and
629 indicating the attainment of temporary steady states following transient accelerations (Carlà
630 et al. 2017b). In contrast, phase 4 declines more gradually but approaches near-zero inverse
631 velocity within ~ 3 months, signalling sustained acceleration towards failure rather than
632 stabilisation. This pattern suggests the slope did not fully recover stability between
633 acceleration episodes, supporting the interpretation of progressive internal degradation and
634 gradual accumulation of strain.

635 While external forcing factors, such as rainfall and seismic activity, modulated the timing and
636 magnitude of these accelerations, they cannot alone explain the observed behaviour. For in-
637 stance, comparable rainfall totals in 2019–2020 did not trigger failure, and acceleration con-
638 tinued through the 2018 dry season. The $1/v$ plots highlight the internal process of material
639 degradation, including microcrack formation and coalescence, leading to the development of
640 a shear surface by March 2020. By observing these behaviours, we demonstrate how dimen-
641 sionless parameters from the wrapped phase can capture meaningful kinematic evolution,
642 offering valuable insight into early destabilisation mechanisms.

643 Finally, it is worth noting that phase 4 is truncated roughly 3 months prior to failure due to
644 increasing noise in the dimensionless measure, preventing observation of the full $1/v$ trend
645 as the landslide approaches collapse. These inverse velocity plots are therefore not intended
646 to predict failure timing but to illustrate the changing kinematic behaviour across acceleration
647 phases.

648

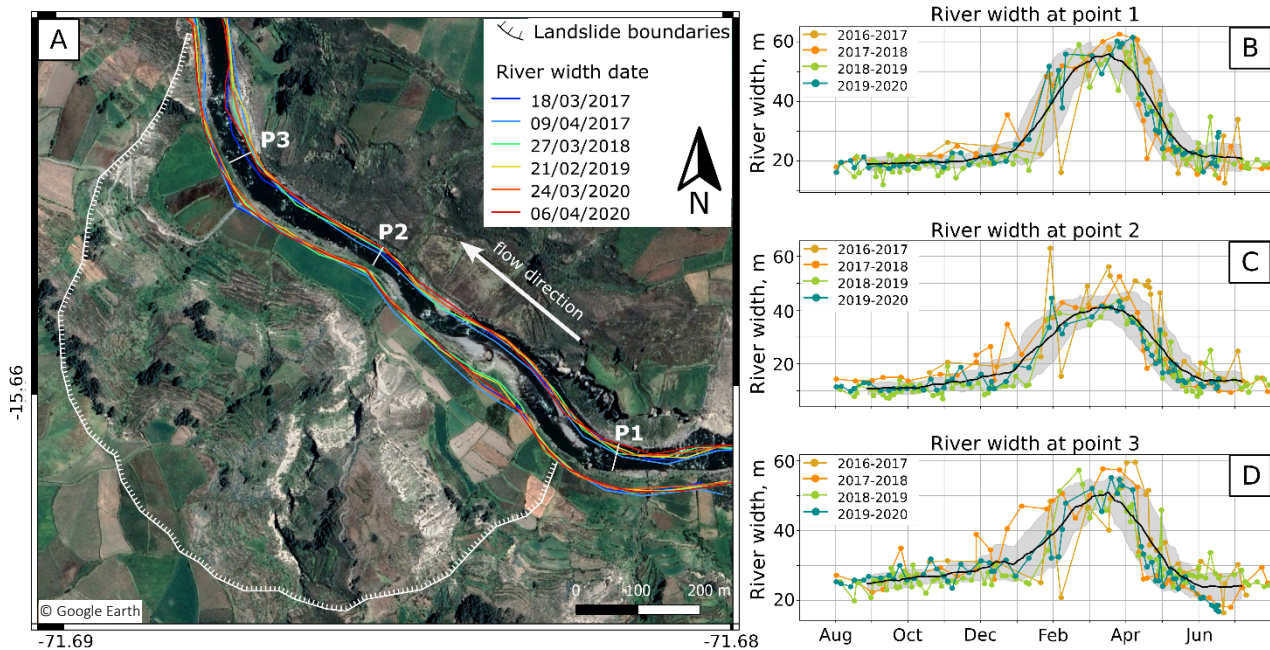


Figure 8. A) Mapping of riverbanks position at maximum width. If date of maximum width differs between P1, P2, P3, multiple dates per wet season are taken (e.g. 2017, 2020). Mapping and annotations are superposed to a ©Google Earth pre-failure (20/04/2019) satellite image. B-D) River widths for P1, P2, P3 respectively. Data is plotted from dry season to dry season the following year. The black curve represents the 40-day running mean, and the grey shading represents one standard deviation above and below the mean.

650 Figure 8A shows the position of the riverbanks during maximum river width periods for each
 651 wet season (2016–2020). Despite potential image resolution limitations, our observations
 652 reveal no clear trend of significant erosion toward the left bank or landslide toe. Instead,
 653 riverbank positions vary over time, indicating movement in both directions, into and away
 654 from the landslide toe. The right bank shows a slight tendency to move away, possibly due to
 655 the landslide toe pushing the riverbed, which may increase erosion on that side. River width
 656 measurements in Figure 8B-D, used as a proxy for erosional power, do not indicate significant
 657 erosion events during the 2020 dry season. These findings suggest that the landslide was not
 658 triggered by high river erosion, but rather by a long-term process of progressive failure.

659

660 5.5. Complementarity

661 Our observations highlight variations in the Achoma landslide's response to triggers,
 662 depending on its stage of basal shear plane maturation, suggesting that different processes
 663 were involved. We retrospectively identify the beginning of a final acceleration already in
 664 January 2020 (as shown by wrapped phase dimensionless activity marker), transitioning into

665 a critical and irreversible instability in March 2020 (as shown by coherence both in space and
666 time), indicating that proactive monitoring could have commenced at least at this critical
667 stage. This finding echoes Jacquemart and Tiampo's (2021) observation of a coherence ratio
668 drop five months before the failure of the Mudcreek landslide, emphasising its potential as
669 early indicator. They also noted that an approach based on time series generation
670 underestimated displacements. In contrast, Handwerger et al. (2019) used a preprocessing
671 step for signal removal before unwrapping in their analysis of the same landslide. Our
672 method, leveraging wrapped phase analysis, offers a more streamlined alternative, providing
673 valuable insights into landslide evolution without complex preprocessing. Unlike traditional
674 InSAR approaches requiring signal removal and reintroduction, our method is less time-
675 consuming and demonstrates the effectiveness of analysing the wrapped phase. In addition
676 to this, integrating InSAR-based signals with optical time series enhances the understanding
677 of landslide dynamics across different phases. The metrics we propose identify areas of
678 incipient strain and early acceleration phases, while optical time series capture the final
679 acceleration phase characterised by larger displacements (Supplementary figure S10).

680 The indicators proposed here rely on the identification of critical features, such as
681 gravitational structures in the coherence signal or the moving mass in the wrapped phase. In
682 practice, wrapped phase patterns could also be used to delineate the boundaries of
683 potentially unstable zones, which can serve as the basis for coherence ratio analyses to assess
684 localised changes relative to their surroundings. While the observed coherence and phase
685 signals are promising indicators, determining whether they can be reliably detected without
686 prior knowledge of landslide locations will require large-scale analysis across diverse terrains,
687 likely combining InSAR with topographic, geomorphic, and signal-specific characteristics.
688 Evaluating the generalisability of this methodology across different landslide types and
689 settings is a key goal for future work. Furthermore, automated detection of these features
690 using machine learning techniques could significantly enhance landslide monitoring.
691 Approaches such as that proposed by Chen et al. (2022) demonstrate the feasibility of
692 applying deep semantic segmentation to recognise active landslides from InSAR.
693 Implementing similar AI-driven frameworks on the precursors identified here could automate
694 the detection of early instability signs, reducing reliance on manual interpretation and
695 providing an efficient first filter for identifying destabilising slopes across large areas. Finally,
696 the approach proposed here could be highly complementary to recent optical monitoring

697 methods aimed at detecting slow-moving landslides. For instance, Van Wyk de Vries et al.
698 (2024) demonstrated that automated Sentinel-2 feature tracking can identify surface
699 deformation for landslides attaining larger velocities than InSAR can detect, providing
700 valuable information on spatial displacement patterns where optical contrast and cloud-free
701 conditions permit. In contrast, InSAR-based coherence and wrapped-phase indicators may be
702 more sensitive to subtler or intermittent deformation and are less dependent on illumination
703 or atmospheric conditions. Furthermore, it is worth noting that the rates of ground deformation
704 detectable with InSAR and optical vary significantly, allowing for the detection of different
705 phases, as shown in this work. Integrating both datasets could therefore improve the
706 detection of a broader spectrum of slope processes, from slow or incipient deformation to
707 more rapid movement phases and enhance confidence in precursor identification by
708 combining independent observational evidence.

709

710

711 **6. Conclusions**

712 Using Sentinel-1 interferograms with non-overlapping short temporal baselines, we identified
713 precursors to the Achoma landslide. Our approach bypasses traditional unwrapping and time
714 series generation, revealing significant spatial coherence loss that indicates gravitational fea-
715 tures linked to strain localisation along the rupture surface, visible five years prior to failure.
716 Intermittent coherence loss from approximately five years to five months before failure sug-
717 gests the progressive development of a hydro-mechanically coupled rupture surface with in-
718 creasing damage concentration. This is further supported by the acceleration, steady-state,
719 and deceleration phases observed in the wrapped phase analysis. Our findings demonstrate
720 the potential of satellite-based InSAR to detect destabilisation precursors before large dis-
721 placements occur, particularly when continuous displacement time series are hindered by
722 land cover or landslide behaviour. By integrating key parameters and their spatiotemporal
723 changes, this methodology could enhance the identification of precursors over larger areas
724 than traditional time series methods alone, making satellite-based monitoring even more val-
725 uable for landslide prediction. However, we acknowledge that not all landslides exhibit meas-
726 urable precursory motion. For example, rapid, shallow failures in unconsolidated materials
727 may occur with little to no detectable warning. The approach presented here is therefore

728 likely applicable to large, complex landslides with long histories of slow deformation for which
729 strain accumulation can be capture, and further research across a broader range of case stud-
730 ies is needed to validate coherence loss patterns as reliable precursors for landslides with
731 minimal ground displacement. In this context, a key next step will be to extend this work to
732 regional studies to capture landslides in diverse geological and climatic settings, with different
733 sizes, mechanisms and material composition, to determine more broadly under which condi-
734 tions similar precursory patterns would emerge and how can they be objectively character-
735 ised.

736 Our findings are nevertheless significant for two practical reasons. First, the Achoma landslide
737 went unnoticed until shortly before failure, a common issue in landslide science where mon-
738 itoring typically begins after events occur rather than during early precursor stages. Identify-
739 ing reliable precursors in satellite data could improve landslide prediction on both local and
740 broader scales. While our analysis demonstrates the potential for satellite-based detec-
741 tion of precursory signals, effective early warning ultimately depends on coupling such
742 remote observations with local monitoring and community awareness. Second, the chal-
743 lenge of monitoring landslides only after failure limits the capture of earlier instability phases.
744 Proactively targeting destabilising slopes for instrumentation is critical for effective hazard
745 assessment, failure prediction, and understanding underlying processes. A complementary
746 approach that combines the strengths of InSAR and optical time series, while leveraging AI
747 for automated feature detection, holds remarkable potential for advancing real-time land-
748 slide monitoring. Such innovations are key to enhancing community resilience by enabling
749 early detection and supporting timely response and preparedness in landslide-prone regions.

750

751

752

753 **Statements and Declarations**

754

755 **Authors Contribution**

756 BD conceived the idea submitted for CNES fellowship application, PL and MPD helped shape
757 the research. PL brought previous knowledge for the case study and contributed to concep-
758 tual ideas. BD and MPD designed the method for InSAR-based precursors. BD generated the

759 codes and carried out the analysis. BD, PL and MPD contributed to interpretation. BD wrote
760 the manuscript, PL and MPD provided critical feedback.

761

762 **Funding**

763 This study was carried out as part of a 2-year CNES funded fellowship to Benedetta Dini. The
764 fellowship was undertaken at ISTerre (Universite Grenoble-Alpes)

765

766 **Competing Interest**

767 The authors declare no competing interests.

768

769 **Data availability**

770 Sentinel-1 SAR data is freely available from the Copernicus Data Browser at
771 <https://browser.dataspace.copernicus.eu/>. Rainfall data are provided by SENAMHI and can
772 be downloaded from <https://www.gob.pe/senamhi>. Seismic data provided by the Instituto
773 Geofísico del Perú are available at <https://www.gob.pe/igp>. PlanetScope images are available
774 from Planet Lab at <https://www.planet.com/>. The processed wrapped interferograms and co-
775 herence images used in this study have been deposited in Zenodo: Dini, B. (2025): Wrapped
776 interferograms and coherence Achoma landslide, <https://zenodo.org/records/17602759>.
777 Auxiliary data and python scripts required to reproduce the analysis presented in this paper
778 are also archived in Zenodo: Dini, B. (2025), Auxiliary data and analysis scripts for the Achoma
779 landslide study, Zenodo, <https://zenodo.org/records/17753976>. All datasets necessary to re-
780 produce the figures and analysis are therefore publicly available.

781

782 References

- 783 Agliardi F, Scuderi MM, Fusi N, Collettini C (2020) Slow-to-fast transition of giant creeping
784 rockslides modulated by undrained loading in basal shear zones. *Nat Commun* 11:1–11
- 785 Akkar S, Bommer JJ (2010) Empirical equations for the prediction of PGA, PGV, and spectral
786 accelerations in Europe, the mediterranean region, and the Middle East. *Seismol Res Lett*
787 81:195–206. <https://doi.org/10.1785/gssrl.81.2.195>
- 788 Badoux A, Graf C, Rhyner J, et al (2009) A debris-flow alarm system for the Alpine Illgraben
789 catchment: design and performance. *Nat hazards* 49:517–539
- 790 Ballantyne CK (1986) Landslides and slope failures in Scotland: A review. *Scott Geogr Mag*
791 102:134–150. <https://doi.org/10.1080/00369228618736667>
- 792 Berardino P, Fornaro G, Lanari R, Sansosti E (2002) A new algorithm for surface deformation
793 monitoring based on small baseline differential SAR interferograms. *IEEE Trans Geosci*
794 *Remote Sens* 40:2375–2383
- 795 Bontemps N, Lacroix P, Larose E, et al (2020) Rain and small earthquakes maintain a slow-
796 moving landslide in a persistent critical state. *Nat Commun* 11:1–10.
797 <https://doi.org/10.1038/s41467-020-14445-3>
- 798 Carey JM, Massey CI, Lyndsell B, Petley DN (2019) Displacement mechanisms of slow-moving
799 landslides in response to changes in porewater pressure and dynamic stress. *Earth Surf*
800 *Dyn* 7:707–722
- 801 Carlà T, Intrieri E, Di Traglia F, et al (2017a) Guidelines on the use of inverse velocity method
802 as a tool for setting alarm thresholds and forecasting landslides and structure collapses.
803 *Landslides* 14:517–534
- 804 Carlà T, Intrieri E, Raspini F, et al (2019) Author Correction: Perspectives on the prediction of
805 catastrophic slope failures from satellite InSAR (*Scientific Reports*, (2019), 9, 1, (14137),
806 10.1038/s41598-019-50792-y). *Sci Rep* 9:1–9. <https://doi.org/10.1038/s41598-019-55024-x>
- 807
- 808 Carlà T, Macciotta R, Hendry M, et al (2017b) Displacement of a landslide retaining wall and
809 application of an enhanced failure forecasting approach.
810 <https://doi.org/10.1007/s10346-017-0887-7>
- 811 **Cheab, A., Lacroix, P., Zerathe, S. et al. Landslides induced by the 2017 Mw7.3**
812 **Sarpol Zahab earthquake (Iran). *Landslides* 19, 603–619 (2022).**
813 **<https://doi.org/10.1007/s10346-021-01832-0>**
- 814 Chen X, Yao X, Zhou Z, et al (2022) DRs-UNet: A Deep Semantic Segmentation Network for the
815 Recognition of Active Landslides from InSAR Imagery in the Three Rivers Region of the
816 Qinghai–Tibet Plateau. *Remote Sens* 14:. <https://doi.org/10.3390/rs14081848>
- 817 Colesanti C, Wasowski J (2006) Investigating landslides with space-borne Synthetic Aperture
818 Radar (SAR) interferometry. *Eng Geol* 88:173–199
- 819 Cook KL, Rekapalli R, Dietze M, et al (2021) Detection and potential early warning of
820 catastrophic flow events with regional seismic networks. *Science* (80-) 374:87–92.
821 <https://doi.org/10.1126/science.abj1227>
- 822 Costantini M, Minati F, Trillo F, et al (2021) European Ground Motion Service (EGMS). In: 2021
823 IEEE International Geoscience and Remote Sensing Symposium IGARSS. pp 3293–3296
- 824 Dini B, Doin M-P, Lacroix P, Gay M (2022) Satellite-based InSAR: application and signal
825 extraction for the detection of landslide precursors, in: *Proceedings of 28th Colloque*
826 *Gretsi*, Nancy, France, 6-9 September 2022, 001-0308, p. 1233-1236
- 827 Dini B, Manconi A, Loew S (2019) Investigation of slope instabilities in NW Bhutan as derived
828 from systematic DInSAR analyses. *Eng Geol* 259:.

829 <https://doi.org/10.1016/j.enggeo.2019.04.008>

830 Dini B, Manconi A, Loew S, Chopel J (2020) The Punatsangchhu-I dam landslide illuminated
831 by InSAR multitemporal analyses. *Sci Rep* 10:8304

832 Doin M-P, Guillaso S, Jolivet R, et al (2011) Presentation of the small baseline NSBAS
833 processing chain on a case example: The Etna deformation monitoring from 2003 to
834 2010 using Envisat data. In: Proceedings of the Fringe symposium. ESA SP-697, Frascati,
835 Italy, pp 3434–3437

836 Fan X, Xu Q, Liu J, et al (2019) Successful early warning and emergency response of a
837 disastrous rockslide in Guizhou province, China. *Landslides* 16:2445–2457

838 Ferretti a, Prati C, Rocca F, et al (2005) Permanent Scatterers technology: a powerful state of
839 the art tool for historic and future monitoring of landslides and other terrain instability
840 phenomena. *Int Conf Landslide Risk Manag 18th Annu Vancouver Geotech Soc Symp* 1–
841 9

842 Ferretti A, Fumagalli A, Novali F, et al (2011) A New Algorithm for Processing Interferometric
843 Data-Stacks: SqueeSAR. *IEEE Trans Geosci Remote Sens* 49:3460–3470.
844 <https://doi.org/10.1109/TGRS.2011.2124465>

845 Ferretti A, Prati C, Rocca F (2001) Permanent scatterers in SAR interferometry. *IEEE Trans*
846 *Geosci Remote Sens* 39:8–20

847 Fiolleau S, Jongmans D, Bièvre G, et al (2020) Seismic characterization of a clay-block rupture
848 in Harmalière landslide, French Western Alps. *Geophys J Int* 221:1777–1788

849 Fourniadis IG, Liu JG, Mason PJ (2007) Regional assessment of landslide impact in the Three
850 Gorges area, China, using ASTER data: Wushan-Zigui. *Landslides* 4:267–278.
851 <https://doi.org/10.1007/s10346-007-0080-5>

852 Froude MJ, Petley DN (2018) Global fatal landslide occurrence from 2004 to 2016. *Nat Hazards*
853 *Earth Syst Sci* 18:2161–2181

854 Guzzetti F (2021) Invited perspectives: Landslide populations—can they be predicted? *Nat*
855 *Hazards Earth Syst Sci* 21:1467–1471

856 Handwerger, A.L., Lacroix, P., Bell, A.F. *et al.* Multi-sensor remote sensing captures
857 geometry and slow-to-fast sliding transition of the 2017 Mud Creek landslide. *Sci*
858 *Rep* **15**, 29831 (2025). <https://doi.org/10.1038/s41598-025-11399-8>

859 Handwerger AL, Huang M, Fielding EJ, et al (2019) OPEN A shift from drought to extreme
860 rainfall drives a stable landslide to catastrophic failure. 1–12.
861 <https://doi.org/10.1038/s41598-018-38300-0>

862 Instituto Geofísico del Peru Instituto Geofísico del Peru. <https://www.gob.pe/igp>. Accessed 1
863 Sep 2022

864 Intrieri E, Raspini F, Fumagalli A, et al (2018) The Maoxian landslide as seen from space:
865 detecting precursors of failure with Sentinel-1 data. *Landslides* 15:123–133

866 Jacquemart M, Tiampo K (2021) Leveraging time series analysis of radar coherence and
867 normalized difference vegetation index ratios to characterize pre-failure activity of the
868 Mud Creek landslide, California. *Nat Hazards Earth Syst Sci* 21:629–642.
869 <https://doi.org/10.5194/nhess-21-629-2021>

870 Kumar V, Venkataraman G (2011) SAR interferometric coherence analysis for snow cover
871 mapping in the western Himalayan region. *Int J Digit Earth* 4:78–90.
872 <https://doi.org/10.1080/17538940903521591>

873 Lacroix P, Berthier E, Maquerhua ET (2015) Earthquake-driven acceleration of slow-moving
874 landslides in the Colca valley, Peru, detected from Pléiades images. *Remote Sens Environ*
875 165:148–158. <https://doi.org/10.1016/j.rse.2015.05.010>

876 Lacroix P, Bièvre G, Pathier E, et al (2018) Use of Sentinel-2 images for the detection of
877 precursory motions before landslide failures. *Remote Sens Environ* 215:507–516.
878 <https://doi.org/10.1016/j.rse.2018.03.042>

879 Lacroix P, Dini B, Cheaib A (2021) Measuring kinematics of slow-moving landslides from
880 satellite images. In: *Displacement measurement by remote sensing Imagery*, Iste-Wiley.
881 London

882 Lacroix P, Gavillon T, Bouchant C, et al (2022) SAR and optical images correlation illuminates
883 post-seismic landslide motion after the Mw 7.8 Gorkha earthquake (Nepal). *Sci Rep*
884 12:6266 <https://doi.org/10.1038/s41598-022-10016-2>

885 Lacroix, P., Dehecq, A. & Taipei, E. Irrigation-triggered landslides in a Peruvian desert
886 caused by modern intensive farming. *Nat. Geosci.* **13**, 56–60 (2020).
887 <https://doi.org/10.1038/s41561-019-0500-x>

888 Lacroix P, Huanca J, Angel LA, Taipei E (2023) Precursory Motion and Time-Of-Failure
889 Prediction of the Achoma Landslide, Peru, From High Frequency PlanetScope Satellites.
890 *Geophys Res Lett* 50:1–11. <https://doi.org/10.1029/2023GL105413>

891 Lacroix P, Perfettini H, Taipei E, Guillier B (2014) Coseismic and postseismic motion of a
892 landslide: Observations, modeling, and analogy with tectonic faults. *Geophys Res Lett*
893 41:6676–6680. <https://doi.org/10.1002/2014GL061170>

894 Li M, Zhang L, Ding C, et al (2020) Retrieval of historical surface displacements of the Baige
895 landslide from time-series SAR observations for retrospective analysis of the collapse
896 event. *Remote Sens Environ* 240:111695. <https://doi.org/10.1016/j.rse.2020.111695>

897 Liu P, Li Z, Hoey T, et al (2013) Using advanced InSAR time series techniques to monitor
898 landslide movements in Badong of the Three Gorges region, China. *Int J Appl Earth Obs*
899 *Geoinf* 21:253–264

900 Loew S, Gschwind S, Gischig V, et al (2017) Monitoring and early warning of the 2012 Preonzo
901 catastrophic rockslope failure. *Landslides* 14:141–154

902 Manconi A (2021) How phase aliasing limits systematic space-borne DInSAR monitoring and
903 failure forecast of alpine landslides. *Eng Geol* 287:106094

904 McColl ST (2022) *Landslide causes and triggers*. Elsevier Inc.

905 Meyer FJ, Sandwell DT (2012) SAR interferometry at Venus for topography and change
906 detection. *Planet Space Sci* 73:130–144.
907 <https://doi.org/https://doi.org/10.1016/j.pss.2012.10.006>

908 Notti D, Meisina C, Zucca F, Colombo A (2012) Models to predict Persistent Scatterers data
909 distribution and their capacity to register movement along the slope. *Proc FRINGE 2011*
910 2011:19–23

911 Palmer J (2017) Creeping catastrophes: Studies of slow landslides could unmask the
912 mechanics of a worldwide scourge. *Nature* 548:384–386.
913 <https://doi.org/10.1038/548384a>

914 Petley D (2012) Global patterns of loss of life from landslides. *Geology* 40:927–930

915 Pham MQ, Lacroix P, Doin MP (2018) Sparsity optimization method for slow-moving landslides
916 detection in satellite image time-series. *IEEE Trans Geosci Remote Sens* 57:2133–2144

917 Roy P, Martha TR, Khanna K, et al (2022) Time and path prediction of landslides using InSAR
918 and flow model. *Remote Sens Environ* 271:112899.
919 <https://doi.org/10.1016/j.rse.2022.112899>

920 Servicio Nacional de Meteorología e Hidrología del Perú Servicio Nacional de Meteorología e
921 Hidrología del Perú. <https://www.gob.pe/senamhi>. Accessed 10 Oct 2023

922 Strozzi T, Caduff R, Jones N, et al (2020) Monitoring rock glacier kinematics with satellite

923 synthetic aperture radar. *Remote Sens* 12:1–24. <https://doi.org/10.3390/rs12030559>

924 Strzabala K, Cwiakala P, Puniach E (2024) Identification of Landslide Precursors for Early
 925 Warning of Hazards with Remote Sensing. *Remote Sens* 16:.
 926 <https://doi.org/10.3390/rs16152781>

927 Thollard F, Clesse D, Doin M-P, et al (2021) FLATSIM: The ForM@Ter LARge-Scale Multi-
 928 Temporal Sentinel-1 Interferometry Service. *Remote Sens*. 13

929 Thouret JC, Wörner G, Gunnell Y, et al (2007) Geochronologic and stratigraphic constraints on
 930 canyon incision and Miocene uplift of the Central Andes in Peru. *Earth Planet Sci Lett*
 931 263:151–166. <https://doi.org/10.1016/j.epsl.2007.07.023>

932 Valletta A, Carri A, Segalini A (2022) Definition and application of a multi-criteria algorithm to
 933 identify landslide acceleration phases. *Georisk Assess Manag Risk Eng Syst Geohazards*
 934 16:555–569

935 Van Wyk de Vries, M., Arrell, K., Basyal, G.K., Densmore, A.L., Dunant, A., Harvey, E.L. et
 936 al. (2024) Detection of slow-moving landslides through automated monitoring of
 937 surface deformation using Sentinel-2 satellite imagery. *Earth Surface Processes and*
 938 *Landforms*, 49(4), 1397–1410. Available from: <https://doi.org/10.1002/esp.5775>

939 Wasowski J, Bovenga F (2022) Chapter 11 - Remote sensing of landslide motion with emphasis
 940 on satellite multi-temporal interferometry applications: an overview. In: Davies T, Rosser
 941 N, Shroder Risks, and Disasters (Second Edition) JFBT-LH (eds) *Hazards and Disasters*
 942 Series. Elsevier, pp 365–438

943 Wasowski J, Bovenga F (2014) Investigating landslides and unstable slopes with satellite Multi
 944 Temporal Interferometry: Current issues and future perspectives. *Eng Geol* 174:103–138

945 Yang W, Fang J, Liu-Zeng J (2021) Landslide-lake outburst floods accelerate downstream slope
 946 slippage. *Earth Surf Dyn Discuss* 2021:1–19

947 Yang W, Wang Y, Sun S, et al (2019) Using Sentinel-2 time series to detect slope movement
 948 before the Jinsha River landslide. *Landslides* 16:1313–1324

949 Zerathe S, Lacroix P, Jongmans D, et al (2016) Morphology, structure and kinematics of a
 950 rainfall controlled slow-moving Andean landslide, Peru. *Earth Surf Process Landforms*
 951 41:1477–1493. <https://doi.org/10.1002/esp.3913>

952 Zhou C, Yin K, Cao Y, et al (2018) Displacement prediction of step-like landslide by applying a
 953 novel kernel extreme learning machine method. *Landslides* 15:2211–2225.
 954 <https://doi.org/10.1007/s10346-018-1022-0>

955